

# 1 Diffusive and Fluidlike Motion of Homochiral Domain Walls in 2 Easy-Plane Magnetic Strips

3 David A. Smith,<sup>1,\*</sup> So Takei,<sup>2,3,†</sup> Bella Brann,<sup>1</sup> Lia Compton,<sup>1</sup>  
4 Fernando Ramos-Diaz,<sup>1</sup> Matthew Simmers,<sup>4</sup> and Satoru Emori<sup>1,‡</sup>

5 <sup>1</sup>*Department of Physics, Virginia Tech, Blacksburg, VA, 24061, U.S.A.*

6 <sup>2</sup>*Department of Physics, Queens College of the City University of New York, Queens, New York, 11367, U.S.A.*

7 <sup>3</sup>*Physics Doctoral Program, The Graduate Center of the City University of New York, New York, New York 10016, U.S.A.*

8 <sup>4</sup>*Academy of Integrated Science, Virginia Tech, Blacksburg, VA, 24061, U.S.A.*

9 (Dated: December 10, 2021)

10 Propagation of easy-plane magnetic precession can enable more efficient spin transport than  
11 conventional spin waves. Such easy-plane spin transport is typically understood in terms of a  
12 hydrodynamic model, partially analogous to superfluids. Here, using micromagnetic simulations,  
13 we examine easy-plane spin transport in magnetic strips as the motion of a train of domain walls  
14 rather than as a hydrodynamic flow. We observe that the motion transitions from diffusive to  
15 fluid-like as the density of domain walls is increased. This transition is most evident in notched  
16 nanostrips, where the the domain walls are pinned by the notch defect in the diffusive regime but  
17 propagate essentially unimpeded in the fluid-like regime. Our findings suggest that spin transport  
18 via easy-plane precession, robust against defects, is achievable in strips based on realistic metallic  
19 ferromagnets and hence amenable to practical device applications.

## 20 I. INTRODUCTION

21 Transport of spin information via magnetization  
22 dynamics is a key area of rapid development within  
23 spintronics [1]. To date, much work on micron-scale spin  
24 transport has focused on using diffusive spin waves [2, 3].  
25 The magnetization precession cone angle in diffusive  
26 spin waves is typically  $\ll 10^\circ$ , and the associated spin  
27 flow decays exponentially with decay length inversely  
28 proportional to the Gilbert damping parameter  $\alpha$ , as  
29 illustrated in Fig. 1(a). As a result, efficient spin  
30 transport at or beyond the micron scale has been difficult  
31 to attain, particularly in typical metallic ferromagnets  
32 with  $\alpha > 10^{-3}$  that are compatible with industrial device  
33 fabrication.

34 An alternative method to achieving long distance spin  
35 transport in the form of spin superfluidity [4–10] has  
36 gathered interest in recent years. In spin superfluidity  
37 the magnetization undergoes easy-plane precession with  
38 a cone angle of  $\approx 90^\circ$ , driven by a current-induced  
39 spin-transfer torque [11–13]. The resulting precessional  
40 dynamics propagates along the ferromagnet in a spiraling  
41 manner, as illustrated in Fig. 1(b), and is protected  
42 from unwinding by the strong easy-plane anisotropy  
43 preventing phase slips [14]. While true superfluidity (i.e.

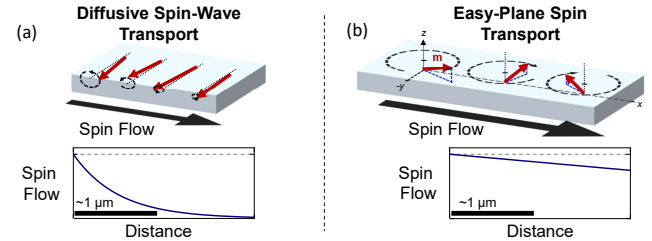


Figure 1. (a) Illustration of small angle precession constituting diffusive spin waves and exponential decay of spin flow. (b) Easy-plane precession constituting superfluid-like spin transport and associated linear decay of spin flow.

44 lossless spin transport) is not possible as a result of ever-  
45 present viscous Gilbert damping, this unique form of  
46 magnetization dynamics creates a spin flow that decays  
47 linearly or algebraically with distance. This easy-plane  
48 superfluid-like spin transport – also called “dissipative  
49 exchange flow” [9] or “exchange-mediated spin transport”  
50 [10] – has been proposed as a means of spin information  
51 transport even in metallic ferromagnets [5, 9, 15–17] with  
52 moderate damping parameters.

53 Halperin and Hohenberg originally proposed a model  
54 to view easy-plane precessional magnetization dynamics  
55 from a hydrodynamic perspective [18], in a manner that  
56 is analogous to that of superfluidity. This hydrodynamic  
57 perspective has been used to analyze easy-plane spin  
58 transport in several studies [9, 16, 17, 19]. However,

\* Correspondence email address: smithd22@vt.edu

† Correspondence email address: So.Takei@qc.cuny.edu

‡ Correspondence email address: semori@vt.edu

59 these studies have focused on the regime that requires  
 60 higher drive current densities,  $J_c$ . The requirement  
 61 of high current densities ( $J_c > 1 \times 10^{12} \text{ A/m}^2$ ) poses  
 62 potential problems in the form of Joule heating as  
 63 well as electromigration altering material properties.  
 64 While studies have investigated the effects of in-plane  
 65 magnetocrystalline anisotropy [9], Gilbert damping [17],  
 66 and void defects [16, 19], how the easy-plane spin  
 67 transport behaves at lower drive current densities, closer  
 68 to the range of experimental feasibility, has yet to be  
 69 answered.

70 In this study, we have performed micromagnetic  
 71 simulations of easy-plane spin transport in synthetic  
 72 antiferromagnet nanostrips, focusing on the low drive  
 73 regime. The synthetic antiferromagnet material  
 74 parameters mimic those of experimentally measured,  
 75 metallic ferromagnets. Instead of taking the conventional  
 76 approach from a hydrodynamic perspective, we study the  
 77 dynamics as a train of interacting, homochiral domain  
 78 walls (DWs) [20]. We find that at low drive current  
 79 densities  $J_c$ , the DWs can be pinned by a notch defect.  
 80 We observe the transition from diffusive motion to fluid-  
 81 like motion as  $J_c$  is increased and the DW density<sub>108</sub>  
 82 increases. The dynamics of the DW train converges to<sub>109</sub>  
 83 that of the established hydrodynamic behavior when the<sub>110</sub>  
 84 DW spacing becomes comparable to the DW width at<sub>111</sub>  
 85  $J_c \simeq 5 \times 10^{11} \text{ A/m}^2$ . In this fluid-like regime, the train<sub>112</sub>  
 86 of DWs are unimpeded by the notch defect. Our results<sub>113</sub>  
 87 suggest that even at moderately low  $J_c$  and with deep<sub>114</sub>  
 88 notch defects, it is feasible to achieve easy-plane spin<sub>115</sub>  
 89 transport in a metallic ferromagnetic system.

## 90 II. SIMULATION DETAILS

91 We have simulated easy-plane spin transport – i.e.,<sub>121</sub>  
 92 motion of a train of spiraling homochiral transverse<sub>122</sub>  
 93 Néel DWs – in magnetic nanostrips using Mumax<sup>3</sup>, an<sub>123</sub>  
 94 open-source GPU accelerated micromagnetic simulation<sub>124</sub>  
 95 package [21]. In single-layer ferromagnetic strips (see<sub>125</sub>  
 96 Appendix A), the moving transverse DWs are unstable<sub>126</sub>  
 97 and transform into vortex DWs [22, 23], which effectively<sub>127</sub>  
 98 constitute phase slips and breakdown of coherent easy-<sub>128</sub>  
 99 plane spin transport. We instead focus here on<sub>129</sub>  
 100 simulations of synthetic antiferromagnetic strips, which<sub>130</sub>  
 101 are composed of two ferromagnetic layers coupled in<sub>131</sub>  
 102 an antiparallel manner [24]. The interlayer-coupled<sub>132</sub>  
 103 magnetic moments reduce dipolar fields at the strip<sub>133</sub>  
 104 edges via flux closure and stabilize transverse Néel DWs<sub>134</sub>  
 105 [25]. Thus, the formation of vortices are suppressed<sub>135</sub>  
 106 and easy-plane spin transport, carried by spiraling<sub>136</sub>  
 107 transverse DWs, remains far more stable in synthetic<sub>137</sub>

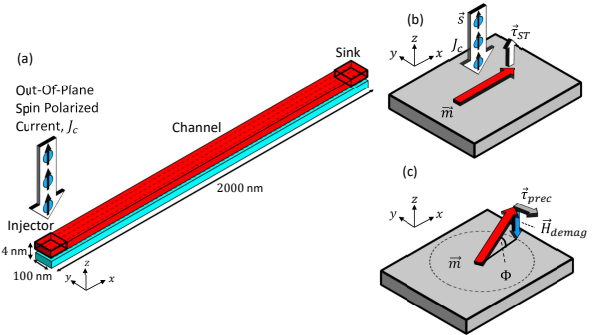


Figure 2. (a) Micromagnetic simulation setup of the synthetic antiferromagnet nanostrip. (b) The resulting torque generated by the out-of-plane spin-polarized electric current  $J_c$ , lifting the magnetization out of the plane in the injector region. (c) The out-of-plane component of the magnetization creates a demagnetizing field, generating a precessional torque that drives easy-plane precession.

antiferromagnets than in single-layer ferromagnets. The enhanced stability of easy-plane spin transport in synthetic antiferromagnets has been previously reported in a micromagnetic study by Skarsvåg *et al.* [7].

A depiction of our simulation set-up is shown in Fig. 2(a). The dimensions of an individual ferromagnetic layer are  $2000 \text{ nm} \times 100 \text{ nm} \times 2 \text{ nm}$  with a cell size of  $2.5 \text{ nm} \times 2.5 \text{ nm} \times 2 \text{ nm}$ . The two layers are coupled using an RKKY interaction with strength  $J_{RKKY} = -1 \text{ mJ/m}^2$ . The initial magnetization states lie completely in plane and are parallel to the long axis of the nanostrip (i.e.  $\vec{m}_i \parallel \pm \hat{x}$ ). To simulate the interaction of easy-plane spin transport with defects, a pair of symmetric, triangular notches with lateral dimensions  $60 \text{ nm} \times 30 \text{ nm}$  were introduced at the midpoint of the nanostrip ( $x = 1000 \text{ nm}$ ).

The material parameters of our nanostrips were chosen to match those of experimentally measured,  $2 \text{ nm}$  thick polycrystalline  $\text{Fe}_{80}\text{V}_{20}$  (see Appendix B for determination of material parameters): saturation magnetization  $M_{sat} = 720 \text{ kA/m}$ , in-plane magnetocrystalline anisotropy  $K = 0 \text{ J/m}^3$ , and Gilbert damping parameter  $\alpha = 0.006$ . The exchange constant was set to  $A_{ex} = 20 \text{ pJ/m}$ , in line with typical literature values for Fe [26, 27]. At each end of the nanostrip in a  $100 \text{ nm} \times 100 \text{ nm}$  region, we introduce an enhancement to the Gilbert damping parameter,  $\alpha' = 0.015$ , to simulate the effects of spin pumping into and out of the nanostrip [28]. The total Gilbert damping parameter in these end regions is  $\alpha_{total} = \alpha + \alpha'$ . All

138 simulations were performed at zero temperature. 186

139 In order to excite dynamics, an out-of-plane spin 187  
 140 polarized charge current density  $J_c$  was applied to the 188  
 141 injection region, as shown in Fig. 2(a). The spin 189  
 142 polarized charge current imparts an out-of-plane spin- 190  
 143 transfer torque [11]  $\vec{\tau}_{ST} \sim \vec{m} \times (\vec{s} \times \vec{m})$ , where  $\vec{s} \parallel \hat{z}$  191  
 144 is the spin polarization, on the magnetization  $\vec{m}$ . This 192  
 145 excitation is similar to that in current-perpendicular-to- 193  
 146 plane perpendicularly magnetized spin valves [12, 13]. 194  
 147 The spin-transfer torque was set to act directly on the top 195  
 148 ferromagnetic layer only. This was done to be consistent 196  
 149 with previous studies [29, 30] showing that injected spins 197  
 150 orthogonal to  $\vec{m}$  in a metallic ferromagnet are absorbed 198  
 151 within the first  $\approx 1$  nm. The spin polarization of the 199  
 152 current was set to  $P = 0.5$ . 200

153 The spin-transfer torque creates a finite out-of-plane 201  
 154 component of the magnetization,  $m_z$ , with an out-of- 202  
 155 plane canting angle  $\Phi$ , shown in Fig. 2(b). The out- 203  
 156 of-plane component  $m_z$  generates a demagnetizing field 204  
 157  $\vec{H}_{demag}$  and a precessional torque  $\vec{\tau}_{prec} \sim -\vec{m} \times \vec{H}_{demag}$ , 205  
 158 as depicted in Fig. 2(c). The torque then causes  $\vec{m}$  206  
 159 to rotate in a constant direction (e.g. clockwise in 207  
 160 the present case) and thus dictates the chirality of the 208  
 161 resulting DWs. The easy-plane magnetization dynamics 209  
 162 then propagates along the nanostrip, away from the 210  
 163 injector, via exchange coupling. 211

### 164 III. RESULTS AND DISCUSSION

#### 165 A. Diffusive Motion of an Isolated Domain Wall

166 In this section, we discuss the behavior of an isolated 216  
 167 DW in both the perfect and notched nanostrips. Both 217  
 168 simulations were performed identically at a charge 218  
 169 current density of  $J_c = 2.4 \times 10^{11}$  A/m<sup>2</sup>. In order to 219  
 170 rotate the magnetization, the energy supplied by the 220  
 171 current-induced spin-transfer torque must overcome the 221  
 172 energy barrier from the uniaxial shape anisotropy of 222  
 173 the nanostrip. This implies a threshold current density 223  
 174 required to excite the dynamics, i.e., inject a DW into the 224  
 175 channel. Additionally when the drive current density is 225  
 176 sufficiently low, only a single DW can be injected into the 226  
 177 nanostrip. When the magnetization is rotated by 180°, a 227  
 178 180° DW is created at the boundary of the source. The 228  
 179 DW is then injected into the nanostrip and driven by the 229  
 180 out-of-plane canting angle  $\Phi$ . 230

181 *Perfect Nanostrip* - We begin with the dynamics 228  
 182 of a single DW injected by the spin polarized 229  
 183 charge current density mechanism mentioned above. 230  
 184 The micromagnetic snapshots in Fig. 3(a) (also see 231  
 185 Supplemental Video 1 [31]) show the isolated DW 232

propagating along the nanostrip and coming to rest in the middle of the nanostrip. This is the point at which the total energy of the system with an isolated DW reaches a local minimum; the spin-transfer torque in the injection region is too weak to overcome the magnetostatically favored configuration where the strip is divided into two oppositely magnetized domains of equal size. The velocity of the isolated DW in the micromagnetic simulations, shown in Fig. 3(c), decays in an exponential, diffusive manner. The simulation data shows an exponential decay time scale of  $\tau = 0.45$  ns.

This diffusive motion (exponentially decaying velocity) of the isolated DW agrees with our one-dimensional analytical model (details given in Appendix C) in which the DW velocity is given by

$$v(t) = \lambda \gamma_K \Phi_0 e^{-\alpha \gamma_K t}. \quad (1)$$

Here  $\lambda \approx 90$  nm is the DW width,  $\gamma_K = \frac{K_\perp}{s(1+\alpha^2)}$  is a rate governed by the strength of the easy-plane anisotropy,  $K_\perp$ , and the spin density,  $s$ ;  $\Phi_0$  is the initial out-of-plane canting angle of the DW. Based on our material parameters our model predicts the velocity decays on a time scale  $\tau = (\alpha \gamma_K)^{-1} = 0.52$  ns. The DW velocity predicted by our model, shown by the dashed blue curve in Fig. 3(c), is in good qualitative agreement with the simulation results.

*Notched Nanostrip* - In the notched nanostrip, the isolated DW also experiences exponentially decaying motion. However, the motion is further complicated by an additional attractive force acting on the DW from the notch defect. The isolated DW propagates towards the notches and upon reaching the notch defect, the DW undergoes damped harmonic oscillations, as seen in Fig. 3(d), eventually becoming pinned at the defect in the center of the nanostrip (see Fig. 3(b) and Supplemental Video 2). These oscillations of the DW about the center of a notch potential have previously been observed experimentally [32].

We conclude that both the perfect and notched nanostrips exhibit qualitatively similar behavior in the sense that the isolated DW is unable to propagate beyond the center of the nanostrip, either as a result of diffusive motion or DW pinning.

#### B. Weakly Interacting Domain Wall Train

Next we consider the motion of a weakly interacting DW train. By increasing the drive charge current density to  $J_c = 3.0 \times 10^{11}$  A/m<sup>2</sup>, multiple DWs can now be injected into the nanostrips, shown in Figs. 4(a,b) and Supplemental Videos 3 and 4.

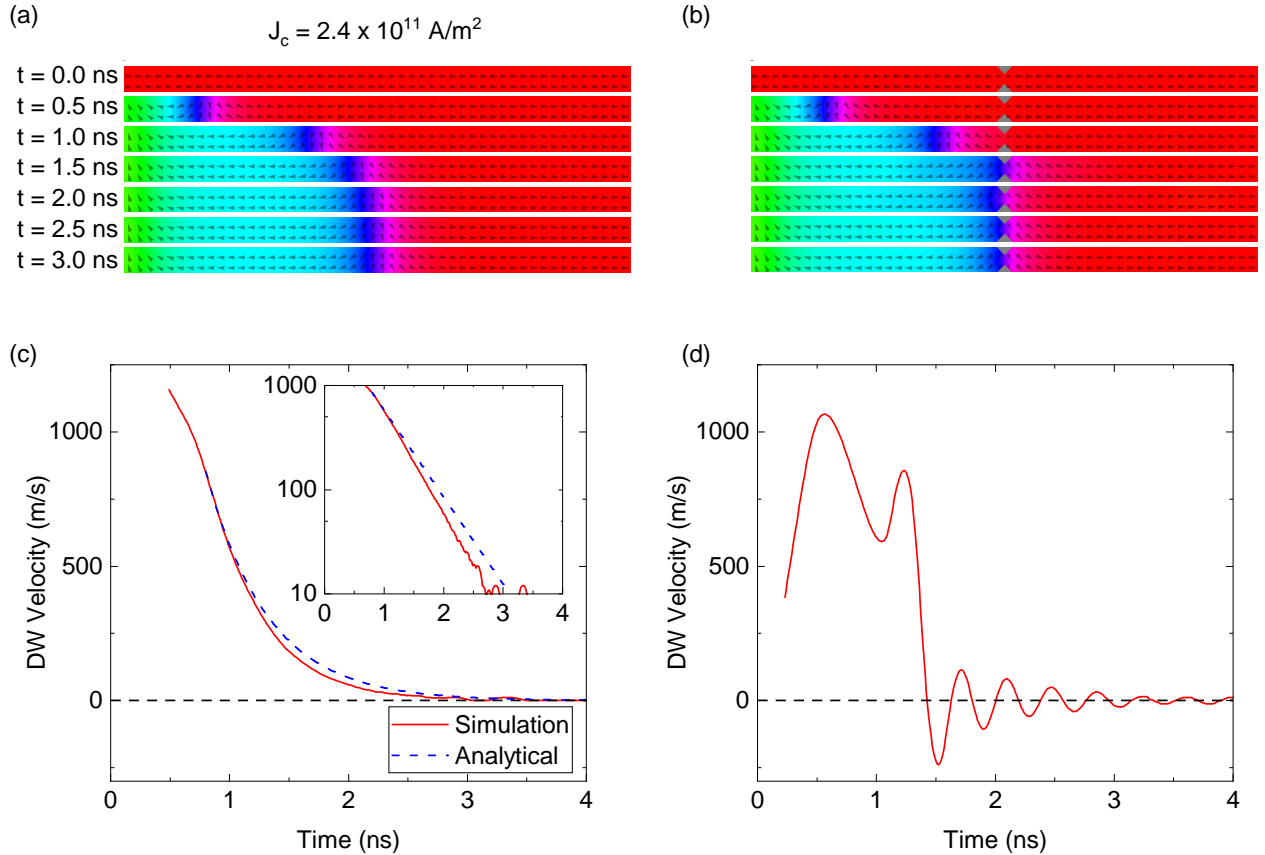


Figure 3. Micromagnetic snapshots of an isolated DW, taken every 0.5 ns from the start of the simulation in the (a) perfect and (b) notched nanostrips. The associated DW velocity as a function of simulation time is shown for the (c) perfect and (d) notched nanostrips. The inset in (c) shows the DW velocity on a logarithmic scale.

*Perfect Nanostrip* - In the perfect nanostrip the DWs<sub>253</sub> individually continue to undergo exponentially decaying<sub>254</sub> motion that is consistent with the behavior predicted by<sub>255</sub> our model. This is shown by the DW velocity averaged<sub>256</sub> across multiple DWs in the simulation in Fig. 4(c) (inset<sub>257</sub> shows average DW velocity on a logarithmic scale).

As multiple DWs are injected into the nanostrip,<sub>259</sub> they interact in a repulsive manner as a result of<sub>260</sub> the homochirality of the DWs [33, 34]. These inter-<sub>261</sub> DW interactions, similar to Coulomb repulsion, become<sub>262</sub> responsible for the movement of the DW train past the<sub>263</sub> middle of the nanostrip. Beyond the center point of<sub>264</sub> the nanostrip, the repulsive interactions are aided by the<sub>265</sub> DWs being attracted to the end of the nanostrip, where<sub>266</sub> they are then annihilated at the sink.

*Notched Nanostrip* - In the notched nanostrip we also<sub>268</sub> observe repulsive DW interactions, but the dynamics is<sub>269</sub> now further complicated due to the notch defect. For<sub>270</sub>  $J_c = 3.0 \times 10^{11} \text{ A/m}^2$ , the first injected DW propagates<sub>271</sub> towards and is pinned at the notch defect, similar to that<sub>272</sub>

of an isolated DW. Meanwhile, additional DWs continue to be injected into the nanostrip, allowing for a series of DWs to build up behind the notch defect. This build-up eventually pushes the first DW through the pinning site, as seen in the micromagnetic snapshots in Fig. 4(b).

Once the leading DW has been pushed through the notch defect, it is attracted to the end of the nanostrip and annihilated. The second DW in the train is pushed along via the inter-DW interactions and then pinned at the notch defect. The corresponding DW velocity for this specific DW is shown in Fig. 4(d). At this point, no additional DWs can be injected into the strip for the remainder of the simulation. The system reaches a steady state where the energy barrier to nucleate DWs is higher than the energy provided by current-induced spin-transfer torque.

We emphasize that the results in Figs. 4(b)(d) and Supplemental Video 4 do not show “fluid-like” dynamics – i.e., the spin transport is not hydrodynamic. Rather than flowing past the constriction as a fluid would, the spin

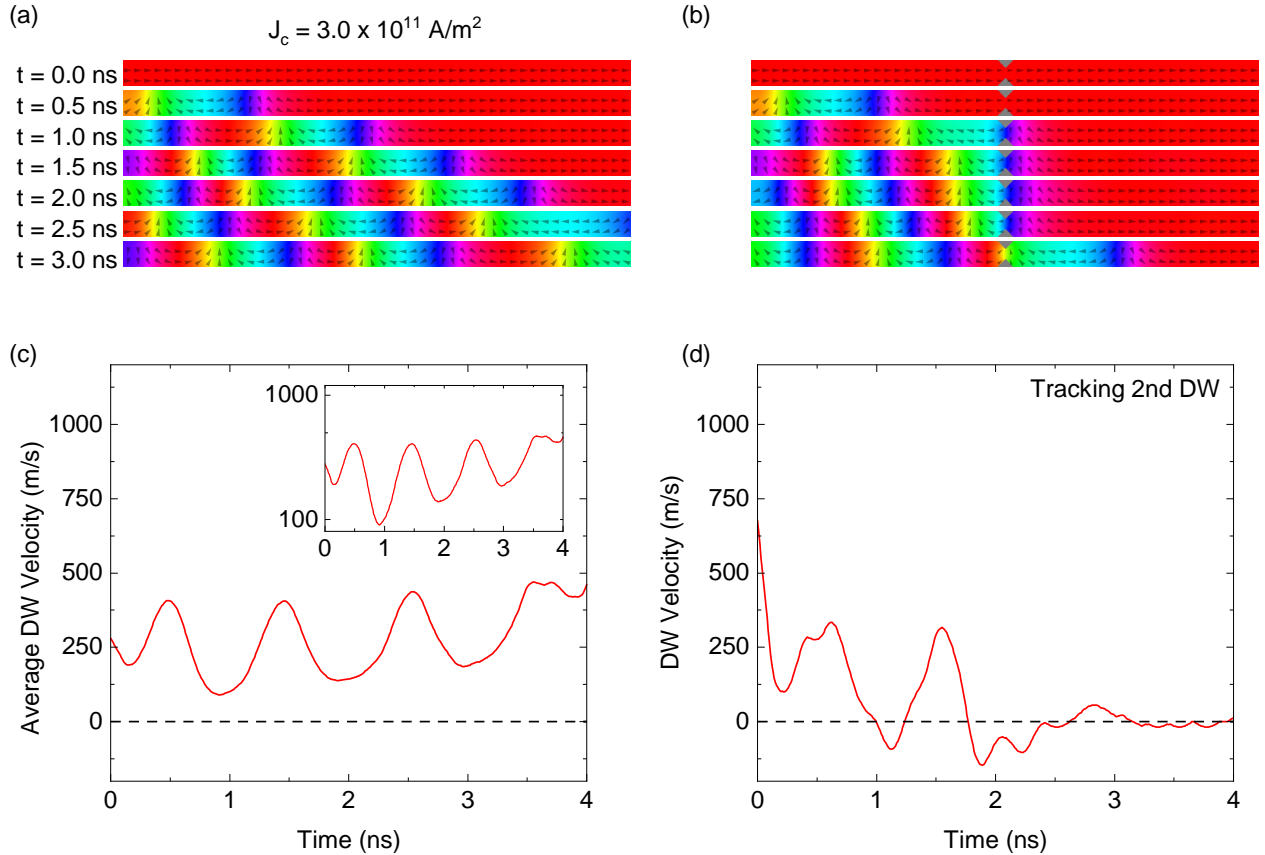


Figure 4. Micromagnetic snapshots of a weakly interacting DW train in the (a) perfect nanostrip and (b) notched nanostrip. In the notched nanostrip, note the momentary pinning of the first DW and the subsequent pinning of the DW train. The average DW velocity as a function of simulation time for the (c) perfect nanostrip and (d) the second DW in the train in the notched nanostrip. The inset in (c) shows the average DW velocity on a logarithmic scale.

273 transport is halted at the defect; the spin-transfer torque<sup>289</sup>  
 274 in the injection region is too weak to nucleate additional<sup>290</sup>  
 275 DWs and propel the train past the defect. Thus, at low<sup>291</sup>  
 276 drives, DW pinning provides a natural way to understand<sup>292</sup>  
 277 the interaction of easy-plane precessional spin transport<sup>293</sup>  
 278 with defects.

### 279 C. Moderately Interacting Domain Wall Train

280 We now increase the charge current density to  $J_c = 4.0 \times 10^{11} \text{ A/m}^2$   
 281 and observe the effect of increased DW<sup>300</sup>  
 282 density on pinning.

283 *Perfect Nanostrip* - The increased current density<sup>302</sup>  
 284 yields behavior similar to that discussed in Sec. III B<sup>303</sup>  
 285 for the perfect nanostrip. The density of the DW train<sup>304</sup>  
 286 increases as more DWs can be injected into the nanostrip,<sup>305</sup>  
 287 see Fig. 5(a) and Supplemental Video 5. The average DW<sup>306</sup>  
 288 velocity, shown in Fig. 5(c), shows a periodic behavior as<sup>307</sup>

294 the DWs are pushed away from trailing walls and slow  
 295 down as they approach the next DW in the train. As a  
 296 result of the increased density of DWs, and thus stronger  
 297 repulsion between neighboring DWs, the average velocity  
 298 is higher than in the case where  $J_c = 3.0 \times 10^{11} \text{ A/m}^2$  (see  
 299 Sec. III B and Figs. 4(a,c)). The continuous motion of the  
 300 DW train shown in Fig. 5(a,c) is beginning to approach the  
 301 fluid-like regime.

302 *Notched Nanostrip* - At  $J_c = 4.0 \times 10^{11} \text{ A/m}^2$ ,  
 303 the pinning of the DW train disappears as a result of  
 304 the stronger inter-DW interactions. The DWs are still  
 305 impeded by the notch defect (Fig. 5(b), Supplemental  
 306 Video 6), evident by the reduction in average DW  
 307 velocity in Fig. 5(d) when compared with the perfect  
 308 nanostrip in Fig. 5(c). However, they are pushed through  
 309 before they can be pinned entirely, allowing for the DW  
 310 train to move continuously throughout the nanostrip.

311 We observe that as the driving current density is  
 312 increased, the density of the DWs increases. The

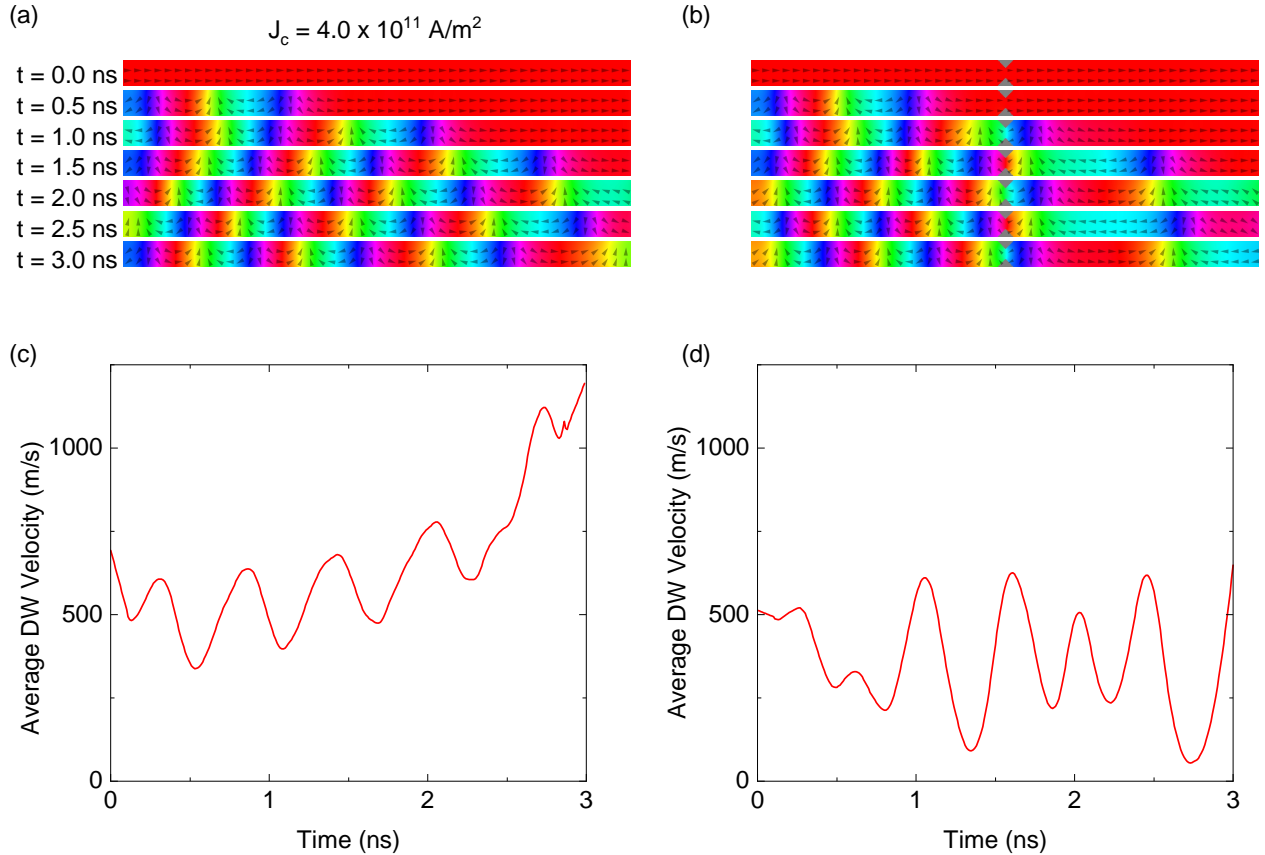


Figure 5. Micromagnetic snapshots of a weakly interacting DW train in the (a) perfect nanostrip and (b) notched nanostrip with the DW interactions are strong enough to overcome the pinning potential. The associated average DW velocity is shown for the (c) perfect and (d) notched nanostrips.

308 increased DW density allows for individual DWs in the 325  
 309 train to be less susceptible to pinning as a result of 326  
 310 the stronger mutual repulsion between the homochiral 327  
 311 DWs. The overall behavior of the magnetization in the 328  
 312 nanostrips starts to approach that of fluid-like dynamics. 329  
 313 This point is further verified by increasing the current 330  
 314 density to higher values, as discussed in the next section. 331

#### 315 D. Strongly Interacting Domain Wall Train

316 Finally, we examine the regime of a strongly 336  
 317 interacting, dense DW train at  $J_c = 8.0 \times 10^{11} \text{ A/m}^2$ . 337  
 318 Micromagnetic snapshots are shown in Figs. 6(a,b), 338  
 319 as well as Supplemental Videos 7 and 8, for the two 339  
 320 geometries.

321 *Perfect Nanostrip* - In the perfect nanostrip, the DW 341  
 322 train has condensed to the point that the DW separation 342  
 323 distance is comparable to the individual DW width  $\sim 343$   
 324 100 nm. At this point, the overall dynamics of the 344

325 nanostrip begins to resemble that of superfluid-like spin  
 326 transport [4–10] in the sense that the magnetization at  
 327 a fixed position is precessing uniformly with simulation  
 328 time. The average DW velocity, shown in Fig. 6(c),  
 329 no longer shows signs of the exponential decay of an  
 330 individual DW. In fact, the DW velocity continues to  
 331 increase as the DW traverses the strip. As they propagate  
 332 further, the DW train begins to separate and individual  
 333 DWs are attracted to the end of the strip where they are  
 334 eventually annihilated.

335 *Notched Nanostrip* - In the notched nanostrip, the  
 336 inter-DW interactions of the dense train have become  
 337 strong enough to overcome the pinning potential well.  
 338 As the DWs impinge on the notch defect, the pinning  
 339 potential reduces the speed of the DW train momentarily,  
 340 before the DWs are pushed through and become  
 341 attracted to the end of the strip and speed up again.  
 342 The reduction in DW velocity from the notch defect can  
 343 be seen clearly in Fig. 6(d). We also note the remarkable  
 344 similarity in average DW velocity between the perfect

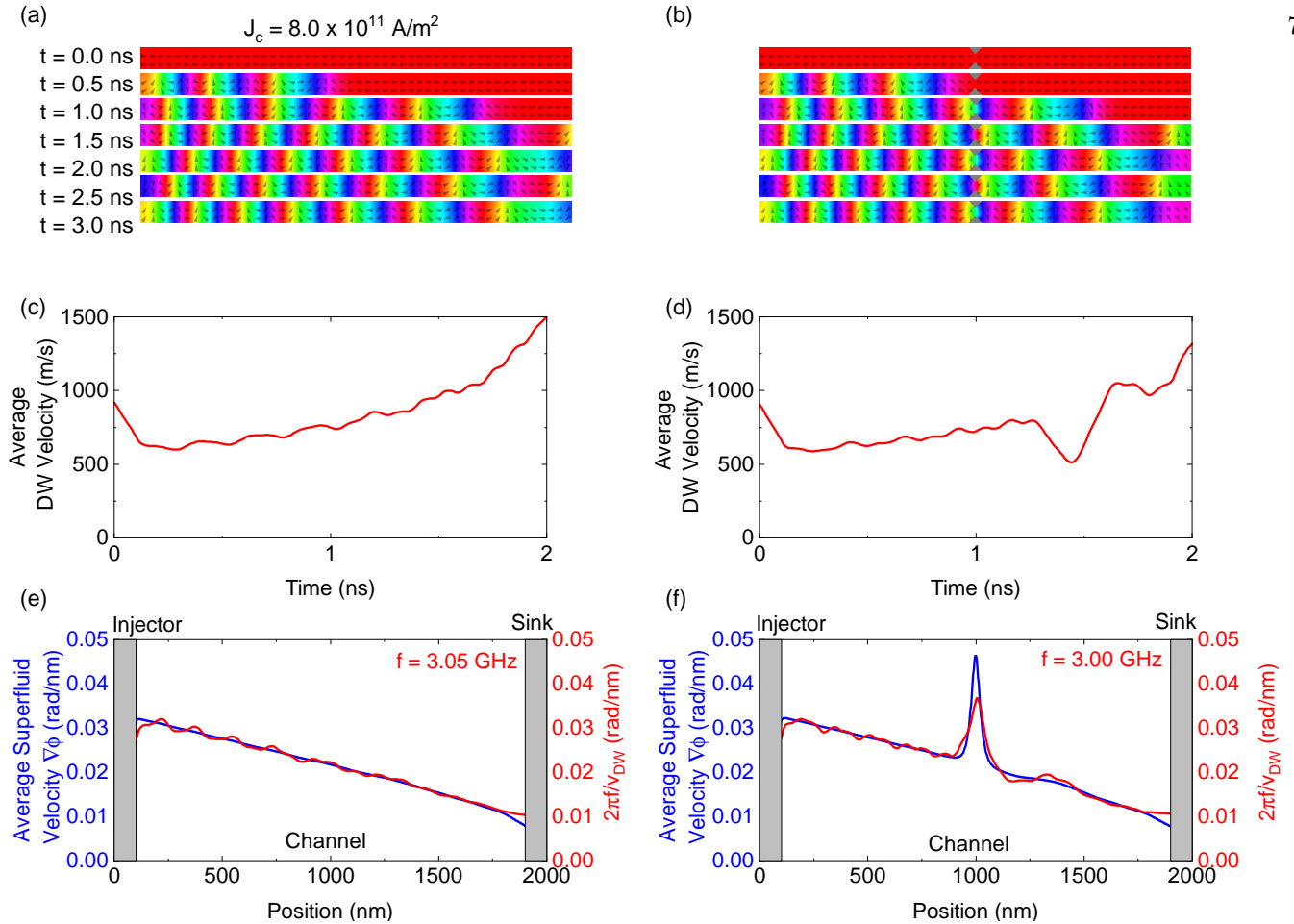


Figure 6. (a), (b) Micromagnetic snapshots of the densely packed DW train that resembles superfluid-like spin transport. (c), (d) The average DW velocity as a function of simulation time for the (c) perfect and (d) notched nanostrips. (e), (f) Time-averaged superfluid velocity and equivalent DW velocity, computed via Eq. 2, as a function of DW position for the (e) perfect and (f) notched nanostrips.

345 and notched nanostrips up to the point of the notch<sup>359</sup>  
 346 defect.<sup>360</sup>

347 *Convergence to Fluid-like Regime* - Our simulation<sup>361</sup>  
 348 results on the motion of a train of DWs showed pinning<sup>362</sup>  
 349 behavior present at lower  $J_c$  in notched nanostrips.<sup>363</sup>  
 350 At sufficiently high  $J_c$ , the pinning behavior vanishes<sup>364</sup>  
 351 and the DW perspective begins to converge with the<sup>365</sup>  
 352 hydrodynamic one. To show further agreement with<sup>366</sup>  
 353 the established hydrodynamic model, we relate the<sup>367</sup>  
 354 DW velocity to the conventional superfluid velocity  $\nabla\phi$ <sup>368</sup>  
 355 (where in the hydrodynamic model the spin current<sup>369</sup>  
 356  $J_s \propto \nabla\phi$  [4]) through the following relationship:<sup>370</sup>

$$\nabla\phi = \frac{2\pi f}{v_{DW}}. \quad (2)$$

357 Here  $\phi$  is the in-plane angle the magnetization makes<sup>373</sup>  
 358 with the  $\hat{x}$  axis,  $\nabla\phi$  is the spatial gradient of  $\phi$  (given<sup>374</sup>

in rad/nm),  $f$  is the precessional frequency of the magnetization, and  $v_{DW}$  is the average DW velocity.

We compute time-averaged  $\nabla\phi$  directly (blue line) at each cell after reaching a steady state and compare it with the equivalent quantity using the average DW velocity (red line) in Fig. 6(e) and Fig. 6(f). We first note the mostly linear decay of  $\nabla\phi$  in the channel, indicating that we are indeed simulating easy-plane spin transport in the fluid-like regime at  $J_c = 8.0 \times 10^{11} \text{ A/m}^2$ . In this fluid-like regime, we find an excellent quantitative agreement between the hydrodynamic and DW perspectives for both the perfect and the notched nanostrips. This agreement confirms that a densely packed DW train behaves as a “fluid” and converges with the hydrodynamic model.

In the notched nanostrips, the rapid increase in  $\nabla\phi$  resulting from the constriction created by the notches

375 is recreated well by our DW perspective. This increase  
 376 in  $\nabla\phi$ , akin to throttling of a fluid, is also in great  
 377 quantitative agreement with the DW perspective: The  
 378 increase in  $\nabla\phi$  corresponding with a reduction in DW  
 379 velocity as the DWs propagate through the notch defect.

### 380 E. Consequences for Practical Applications

381 We now comment on the impacts our simulation results  
 382 would have on experimental realizations of easy-plane  
 383 precessional dynamics. In Fig. 7(a) we compare the time-  
 384 averaged superfluid velocity  $\nabla\phi$  as a function of charge  
 385 current density  $J_c$ . The superfluid velocity shown in  
 386 Fig. 7(a) was computed at  $x = 1500$  nm, beyond the  
 387 location of the notch defect, for both the perfect and  
 388 notched nanostrips.

389 At low values of  $J_c$  ( $< 5 \times 10^{11}$  A/m<sup>2</sup>), we note  
 390 a difference in the superfluid velocity between the two  
 391 geometries. This is a result of pinning by the notch  
 392 defect, impeding individual DWs within the train. The  
 393 pinning behavior disappears with increasing  $J_c$  and  
 394 the superfluid velocities in the two geometries become  
 395 indistinguishable. Thus, at sufficiently high  $J_c$ , the notch  
 396 defect evidently has no effect on the global dynamics of  
 397 easy-plane precession. Remarkably the pinning vanishes  
 398 despite the rather large size of the defect; at their  
 399 deepest point, the pair of notches occupy 60% of the  
 400 nanostrip's width, much larger than the typical edge  
 401 roughness that results from lithographic patterning [35].  
 402 The robust transport, unaffected by such deep notches, is  
 403 promising for achieving easy-plane precessional dynamics  
 404 in lithographically patterned nanostrips.

405 To determine the equivalent DW velocity using Eq. 2,  
 406 the precessional frequency  $f$  of the magnetization is  
 407 determined using a fast Fourier transform on  $m_x$  as  
 408 a function of time along the length of the nanostrip.  
 409 We limit our determination of  $f$  to the fluid-like  
 410 regime in which  $f$  is uniform throughout the nanostrip.<sup>421</sup>  
 411 Precessional frequency and equivalent DW velocity as<sup>425</sup>  
 412 a function of  $J_c$  are plotted in Fig. 7(b) and Fig. 7(c),<sup>426</sup>  
 413 respectively. The superfluid velocity  $\nabla\phi$  and precessional<sup>427</sup>  
 414 frequency  $f$  continuously increase with  $J_c$  but the DW<sup>428</sup>  
 415 velocity saturates at  $\approx 1500$  m/s. This saturation value<sup>429</sup>  
 416 is much higher than the typical experimentally measured<sup>430</sup>  
 417 value in in-plane magnetized strips [22, 25, 36], yet<sup>431</sup>  
 418 well below the maximum magnon group velocity in our<sup>432</sup>  
 419 system of  $\approx 8000$  m/s (derived from a micromagnetically<sup>433</sup>  
 420 computed magnon dispersion curve), which has been<sup>434</sup>  
 421 suggested to be the upper limit on DW velocity [37].<sup>435</sup>  
 422 Instead of being limited by the magnon group velocity,<sup>436</sup>  
 423 the upper bound of the DW speed in our case appears to<sup>437</sup>

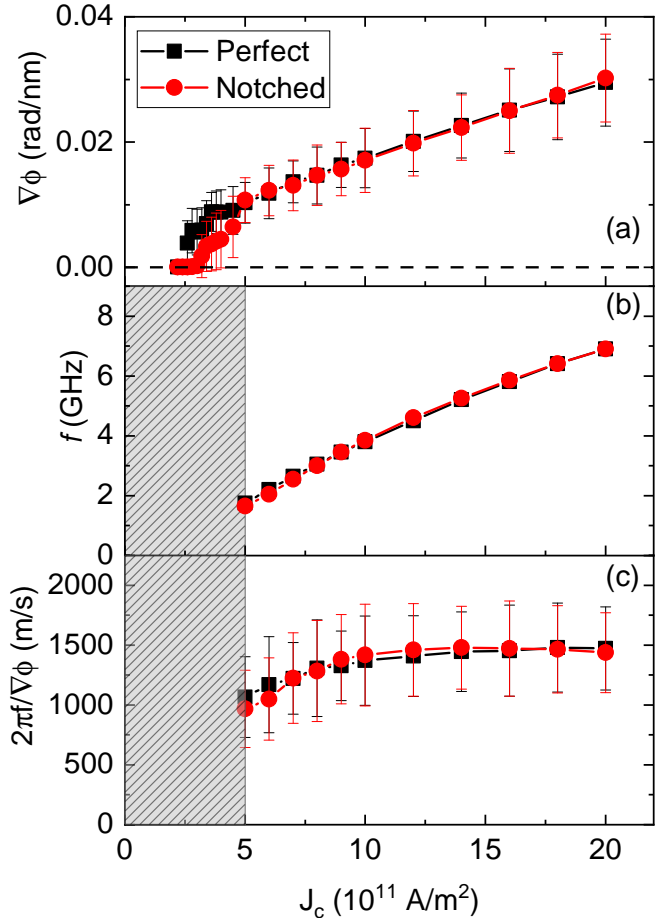


Figure 7. (a) Time-averaged superfluid velocity at  $x = 1500$  nm as a function of driving current density  $J_c$  for the perfect (black squares) and notched (red circles) nanostrips. The error bars indicate the standard deviation. (b) Precessional frequency of the magnetization. (c) Equivalent DW velocity computed using Eq. 2 at  $x = 1500$  nm

be closer to the minimum magnon phase velocity ( $\approx 2000$  m/s), which previously has been shown to restrict the speed of a single transverse Néel DW [38].

Our material parameters were chosen based on experimentally measured thin films of Fe<sub>80</sub>V<sub>20</sub> with  $\alpha = 0.006$  (see Appendix B). This choice is in contrast to the typically chosen insulating ferrimagnetic oxide of yttrium iron garnet (YIG) with  $\alpha \sim 10^{-5} - 10^{-4}$ . However, YIG is notoriously challenging to grow and integrate into practical devices, as it requires fine control of deposition parameters and high processing temperatures. FeV alloys were chosen for their low-loss magnetic properties [39] and compatibility with CMOS-friendly Si substrates when deposited at room

438 temperature [40]. Even though FeV alloys possess a 475  
 439 damping parameter an order of magnitude larger than 476  
 440 YIG, we were able to simulate fluid-like easy-plane 477  
 441 spin transport at moderately achievable current densities 478  
 442 (defined as when  $\nabla\phi$  is the same for both the perfect and 479  
 443 notched nanostrips, via Fig. 7(a)) at  $J_c = 5.0 \times 10^{11}$  480  
 444 A/m<sup>2</sup>. At lower current densities,  $J_c \approx 3 \times 10^{11}$  A/m<sup>2</sup>,  
 445 the DW train could overcome pinning and was able to  
 446 propagate throughout the entirety of the nanostrip. This 481  
 447 would still allow for spin transport along the nanostrip  
 448 (as a result of the rotating magnetization in the spin 482  
 449 sink region) and the possibility of efficient micron-scale 483  
 450 transmission of spin-based information. 484

451 Our chosen method of excitation simulates a current-485  
 452 perpendicular-to-plane spin valve nanopillar with an 486  
 453 out-of-plane polarizer. This is a well established 487  
 454 technique in orthogonal spin-torque oscillators [13]. 488  
 455 Thus, the simulated dynamics here in principle can be 489  
 456 achieved using experimentally proven physics and device 490  
 457 structures. Additionally, recent studies have pointed to 491  
 458 the possibility of in-plane magnetized films producing an 492  
 459 out-of-plane spin torque [41, 42]. This out-of-plane spin- 493  
 460 orbit torque could prove to be a viable method of exciting 494  
 461 easy-plane precessional dynamics as it would eliminate 495  
 462 the need for complicated fabrication of nanopillar spin 496  
 463 valves. However, it is unclear at this time if this 497  
 464 torque would be strong enough to drive the easy-plane 498  
 465 precession dynamics simulated here.

466 It is worth pointing out that while our simulations were 498  
 467 performed at zero temperature, experimental attempts at  
 468 achieving easy-plane precessional dynamics will be done 499  
 469 at finite temperatures. Finite temperatures allow for the 500  
 470 emergence of diffusive thermal magnon transport, which 501  
 471 could couple to the easy-plane spin transport and provide 502  
 472 another avenue for dissipation that is not captured by the 503  
 473 Gilbert damping parameter [43]. In our zero-temperature 504  
 474 simulations, there are no thermal magnons that could 505

give rise to the additional non-Gilbert dissipation. While possible dissipation pathways via thermal magnons are beyond the scope of this present work, future studies employing finite-temperature micromagnetic simulations may give insights into such dissipation in easy-plane spin transport.

#### IV. CONCLUSION

We performed micromagnetic simulations on the interaction of homochiral DW transport via easy-plane precession in synthetic antiferromagnet nanostrips with and without a notch defect. We observed the diffusive motion of an isolated DW and subsequent pinning at the notch defect at low  $J_c$ . With increasing  $J_c$  multiple DWs are injected into the nanostrip, and we observed the crossover to a fluid-like, densely packed DW train. The densely packed DW train in notched nanostrips is robust to edge defects and shows no difference to the perfect nanostrips in the fluid-like regime. Our simulations, with material parameters taken directly from experimentally measured metallic ferromagnets, demonstrate promise for an experimental realization of easy-plane precession at reasonable current densities for efficient micron-scale spin transport.

#### V. ACKNOWLEDGEMENTS

D.A.S., L.C., F.R.-D., and S.E. acknowledge support by NSF Grant No. DMR-2003914. S.T. acknowledges support by CUNY Research Foundation Project # 90922-07 10 and PSC-CUNY Research Award Program # 63515-00 51. M.S. acknowledges support by the Luther and Alice Hamlett Undergraduate Research Support Program.

---

506 [1] D. Sander, Sergio O. Valenzuela, D. Makarov, C. H. 517  
 507 Marrows, E. E. Fullerton, P. Fischer, J. McCord, 518  
 508 P. Vavassori, S. Mangin, P. Pirro, B. Hillebrands, A. D. 519  
 509 Kent, T. Jungwirth, O. Gutfleisch, C. G. Kim, and 520  
 510 A. Berger, “The 2017 Magnetism Roadmap,” Journal of 521  
 511 Physics D: Applied Physics **50**, 363001 (2017). 522

512 [2] R. Lebrun, A. Ross, S. A. Bender, A. Qaiumzadeh, 523  
 513 L. Baldrati, J. Cramer, A. Brataas, R. A. Duine, and 524  
 514 M. Kläui, “Tunable long-distance spin transport in a 525  
 515 crystalline antiferromagnetic iron oxide,” Nature **561**, 526  
 516 222 (2018). 527

517 [3] Brandon L. Giles, Zihao Yang, John S. Jamison, and 528  
 518 Roberto C. Myers, “Long-range pure magnon spin 529  
 519 diffusion observed in a nonlocal spin-Seebeck geometry,” 530  
 520 Physical Review B **92**, 224415 (2015).

521 [4] E B Sonin, “Spin currents and spin superfluidity,” 531  
 522 Advances in Physics **59**, 181 (2010).

523 [5] Hua Chen, Andrew D Kent, Allan H Macdonald, and 532  
 524 Inti Sodemann, “Nonlocal transport mediated by spin 533  
 525 supercurrents,” Physical Review B **90**, 220401(R) (2014).

526 [6] So Takei, Bertrand I Halperin, Amir Yacoby, and 534  
 527 Yaroslav Tserkovnyak, “Superfluid spin transport 535  
 528 through antiferromagnetic insulators,” Physical Review

529 B **90**, 94408 (2014). 586

530 [7] Hans Skarsvåg, Cecilia Holmqvist, and Arne Brataas, 587

531 “Spin Superfluidity and Long-Range Transport in Thin-588

532 Film Ferromagnets,” Physical Review Letters **115**, 589

533 237201 (2015). 590

534 [8] Yaroslav Tserkovnyak, “Perspective: (Beyond) spin-591

535 transport in insulators,” Journal of Applied Physics **124**, 592

536 190901 (2018). 593

537 [9] Ezio Iacocca, T. J. Silva, and Mark A. Hoefer, 594

538 “Symmetry-broken dissipative exchange flows in thin-film-595

539 ferromagnets with in-plane anisotropy,” Physical Review 596

540 B **96**, 134434 (2017). 597

541 [10] T Schneider, D Hill, A Kákay, K Lenz, J Lindner, 598

542 J Fassbender, P Upadhyaya, Yuxiang Liu, Kang Wang, 599

543 Y Tserkovnyak, I N Krivorotov, and I Barsukov, “Self-600

544 stabilizing exchange-mediated spin transport,” Physical 601

545 Review B **103**, 144412 (2021). 602

546 [11] Arne Brataas, Andrew D Kent, and Hideo Ohno, 603

547 “Current-induced torques in magnetic materials,” Nature 604

548 Materials **11**, 372 (2012). 605

549 [12] J. C. Slonczewski, “Current-driven excitation of magnetic 606

550 multilayers,” Journal of Magnetism and Magnetic 607

551 Materials **159**, L1 (1996). 608

552 [13] D Houssameddine, U Ebels, B Dela, B Rodmacq, 609

553 I Firastrau, F Ponthier, M Brunet, C Thirion, J-P-610

554 Michel, L Prejbeanu-buda, M-c Cyrille, O Redon, and 611

555 B Dieny, “Spin-torque oscillator using a perpendicular 612

556 polarizer and a planar free layer,” Nature Materials **6**, 613

557 447 (2007). 614

558 [14] Kwon Kim, So Takei, and Yaroslav Tserkovnyak, 615

559 “Thermally activated phase slips in superfluid spin-616

560 transport in magnetic wires,” Physical Review B **93**, 617

561 020402(R) (2016). 618

562 [15] Jürgen König, Martin Chr Bønsager, and A H-619

563 Macdonald, “Dissipationless Spin Transport in Thin 620

564 Film Ferromagnets,” Physical Review Letters **87**, 187202 621

565 (2001). 622

566 [16] Ezio Iacocca, T J Silva, and Mark A Hoefer, “Breaking 623

567 of Galilean Invariance in the Hydrodynamic Formulation 624

568 of Ferromagnetic Thin Films,” Physical Review Letters 625

569 **118**, 017203 (2017). 626

570 [17] Ezio Iacocca and Mark A. Hoefer, “Hydrodynamic 627

571 description of long-distance spin transport through 628

572 noncollinear magnetization states: Role of dispersion, 629

573 nonlinearity, and damping,” Physical Review B **99**, 630

574 184402 (2019). 631

575 [18] B. I. Halperin and P. C. Hohenberg, “Hydrodynamic 632

576 theory of spinwaves,” Physical Review **188**, 898 (1969). 633

577 [19] Ezio Iacocca, “Controllable vortex shedding from 634

578 dissipative exchange flows in ferromagnetic channels,” 635

579 Physical Review B **102**, 224403 (2020). 636

580 [20] Se Kwon Kim and Yaroslav Tserkovnyak, “Magnetic 637

581 Domain Walls as Hosts of Spin Superfluids and 638

582 Generators of Skyrmions,” Physical Review Letters **119**, 639

583 047202 (2017). 640

584 [21] Arne Vansteenkiste, Jonathan Leliaert, Mykola Dvornik, 641

585 Mathias Helsen, Felipe Garcia-Sanchez, and Bartel Van 642

586 Waeyenberge, “The design and verification of MuMax3,” 643

587 AIP Advances **4**, 107133 (2014).

588 [22] Geoffrey S D Beach, Corneliu Nistor, Carl Knutson, 644

589 Maxim Tsoi, and James L Erskine, “Dynamics of 645

590 field-driven domain-wall propagation in ferromagnetic 646

591 nanowires,” Nature Materials **4**, 741 (2005).

592 [23] A. Mougins, M. Cormier, J. P. Adam, P. J. Metaxas, 647

593 and J. Ferré, “Domain wall mobility, stability and Walker 648

594 breakdown in magnetic nanowires,” Europhysics Letters 649

595 **78**, 57007 (2007).

596 [24] R. A. Duine, Kyung Jin Lee, Stuart S.P. Parkin, and 650

597 M. D. Stiles, “Synthetic antiferromagnetic spintronics,” 651

598 Nature Physics **14**, 217–219 (2018).

599 [25] Serban Lepadatu, Henri Saarikoski, Robert Beacham, 652

600 Maria Jose Benitez, Thomas A. Moore, Gavin Burnell, 653

601 Satoshi Sugimoto, Daniel Yesudas, May C. Wheeler, 654

602 Jorge Miguel, Sarnjeet S. Dhesi, Damien McGrouther, 655

603 Stephen McVitie, Gen Tatara, and Christopher H. 656

604 Marrows, “Synthetic ferrimagnet nanowires with very low 657

605 critical current density for coupled domain wall motion,” 658

606 Scientific Reports **7**, 1640 (2017).

607 [26] F S Ma, H S Lim, Z K Wang, S N Piramanayagam, 659

608 S C Ng, and M H Kuok, “Micromagnetic study of 660

609 spin wave propagation in bicomponent magnonic crystal 661

610 waveguides,” Applied Physics Letters **98**, 153107 (2011).

611 [27] Kodai Niitsu, “Temperature dependence of magnetic 662

612 exchange stiffness in iron and nickel,” Journal of Physics 663

613 D: Applied Physics **53**, 39LT01 (2020).

614 [28] Andrew J Berger, Eric R J Edwards, Hans T 664

615 Nembach, Olof Karis, Mathias Weiler, and T J Silva, 665

616 “Determination of the spin Hall effect and the spin 666

617 diffusion length of Pt from self-consistent fitting of 667

618 damping enhancement and inverse spin-orbit torque 668

619 measurements,” Physical Review B **98**, 244402 (2018).

620 [29] A. Ghosh, S. Auffret, U. Ebels, and W. E. Bailey, 669

621 “Penetration Depth of Transverse Spin Current in 670

622 Ultrathin Ferromagnets,” Physical Review Letters **109**, 671

623 127202 (2012).

624 [30] Youngmin Lim, Behrouz Khodadadi, Jie-Fang Li, Dwight 672

625 Viehland, Aurelien Manchon, and Satoru Emori, 673

626 “Dephasing of transverse spin current in ferrimagnetic 674

627 alloys,” Physical Review B **103**, 024443 (2021).

628 [31] See Supplemental Material at (URL to be provided by 675

629 publisher) for videos depicting magnetization dynamics 676

630 in the various regimes discussed.

631 [32] Eiji Saitoh, Hideki Miyajima, Takehiro Yamaoka, and 677

632 Gen Tatara, “Current-induced resonance and mass 678

633 determination of a single magnetic domain wall,” Nature 679

634 **432**, 203 (2004).

635 [33] Benjamin Kruger, “The interaction of transverse domain 680

636 walls,” Journal of Physics: Condensed Matter **24**, 024209 681

637 (2012).

638 [34] Youngman Jang, S R Bowden, Mark Mascaro, J Unguris, 682

639 and C A Ross, “Formation and structure of 360 and 540 683

640 degree domain walls in thin magnetic strips,” Applied 684

641 Physics Letters **100**, 062407 (2012).

[35] S Dutta, S A Siddiqui, J A Curryan-Incorvia, C A Ross, and M A Baldo, "Micromagnetic modeling of domain wall motion in sub-100-nm-wide wires with individual and periodic edge defects," *AIP Advances* **5**, 127206 (2015).

[36] Stuart S P Parkin, Masamitsu Hayashi, and Luc Thomas, "Magnetic Domain-Wall Racetrack Memory," *Science* **320**, 190 (2008).

[37] Lucas Caretta, Se-Hyeok Oh, Takian Fakhru, Dong-Kyu Lee, Byung Hun Lee, Kwon Kim, Caroline A Ross, Kyung-Jin Lee, and Geoffrey S D Beach, "Relativistic kinematics of a magnetic soliton," *Science* **370**, 1438 (2020).

[38] Ming Yan, Christian Andreas, Attila Kákay, Felipe García-Sánchez, and Riccardo Hertel, "Fast domain wall dynamics in magnetic nanotubes: Suppression of Walker breakdown an Cherenkov-like spin wave emission," *Applied Physics Letters* **99**, 122505 (2011).

[39] David A Smith, Anish Rai, Youngmin Lim, Timothy Q Hartnett, Arjun Sapkota, Abhishek Srivastava, Claudia Mewes, Zijian Jiang, Michael Clavel, Mantu K Hudait, Dwight D Viehland, Jean J Heremans, Prasanna V Balachandran, Tim Mewes, and Satoru Emori, "Magnetic Damping in Epitaxial Iron Alloyed with Vanadium and Aluminum," *Physical Review Applied* **14**, 034042 (2020).

[40] Monika Arora, Erna K Delczeg-Czirjak, Grant Riley, T J Silva, Hans T Nembach, Olle Eriksson, and Justin M Shaw, "Magnetic Damping in Polycrystalline Thin-Film Fe-V Alloys," *Physical Review Applied* **15**, 054031 (2021).

[41] Seung Heon C. Baek, Vivek P. Amin, Young Wan Oh, Gyungchoon Go, Seung Jae Lee, Geun Hee Lee, Kab Jin Kim, M. D. Stiles, Byong Guk Park, and Kyung Jin Lee, "Spin currents and spin-orbit torques in ferromagnetic trilayers," *Nature Materials* **17**, 509 (2018).

[42] D MacNeill, G M Stiehl, M H D Guimaraes, R A Buhrman, J Park, and D C Ralph, "Control of spin-orbit torques through crystal symmetry in WTe<sub>2</sub> /ferromagnet bilayers," *Nature Physics* **13**, 300 (2017).

[43] E B Sonin, "Superfluid spin transport in ferro- and antiferromagnets," *Physical Review B* **99**, 104423 (2019).

[44] Charles Kittel, "On the theory of ferromagnetic resonance absorption," *Physical Review* **73**, 155 (1948).

[45] B. Heinrich, "Spin Relaxation in Magnetic Metallic Layers and Multilayers," in *Ultrathin Magnetic Structures III* (Springer-Verlag, Berlin/Heidelberg, 2005) pp. 143–210.

[46] N L Schryer and L R Walker, "The motion of 180° domain walls in uniform dc magnetic fields," *Journal of Applied Physics* **45**, 5406 (1974).

[47] O A Tretiakov, D Clarke, Gia-Wei Chern, Ya B Bazaliy, and O Tchernyshyov, "Dynamics of Domain Walls in Magnetic Nanostrips," *Physical Review Letters* **100**, 127204 (2008).

## Appendix A: Easy-plane Precession Dynamics in Single Layer Systems

We focused on simulating easy-plane spin transport in synthetic antiferromagnets as opposed to single layer nanostrips. In synthetic antiferromagnets, the long-range dipolar fields from one ferromagnetic layer are compensated by an adjacent second layer. This has the effect of stabilizing transverse Néel DWs and suppressing Walker breakdown [25]. Micromagnetic snapshots of phase slips via vortex formation (similar to Walker breakdown) in single layer systems are shown in Fig. 8(a) and Fig. 8(b) for the perfect and notched nanostrips, respectively. Supplemental Videos 9 and 10 complement the micromagnetic snapshots shown in Figs. 8(a,b).

In the perfect nanostrip, a vortex core begins to form at the end of the nanostrip within a DW. The vortex core then propagates against the flow of DWs. In the notched nanostrips, multiple vortex cores begin to form at the edges of the nanostrip, similar to the perfect nanostrip. The vortex fully forms off the tip of the notch defect (see Supplemental Video 10). These vortices stay in the nanostrip until they encounter a vortex with opposite core polarity upon which the pair is annihilated.

The difference between the single layer (Fig. 8) and synthetic antiferromagnet systems (Fig. 4) is striking. The formation of vortices is absent in synthetic antiferromagnet systems up to high drive current densities  $J_c \gtrsim 2 \times 10^{12} \text{ A/m}^2$ , even in notched nanostrips.

## Appendix B: Experimental Determination of Material Parameters

The material parameter chosen for our micromagnetic simulations were similar to those of experimentally measured polycrystalline Fe<sub>80</sub>V<sub>20</sub> thin films. We deposited these films using magnetron sputtering with base pressure  $< 5 \times 10^{-8} \text{ Torr}$ . The films were deposited on Si/SiO<sub>2</sub> substrates at room temperature with an Ar pressure of 3 mTorr. A Ti/Cu seed layer was initially deposited to promote good adhesion to the substrate and a Ti capping layer was deposited to protect against film oxidation. Fe and V were co-sputtered from two separate targets. All material deposition rates were calibrated using x-ray reflectivity. The sample stack structure is sub./Ti(3)/Cu(3)/Fe<sub>80</sub>V<sub>20</sub>(2)/Ti(3) where the values in the parentheses are layer thicknesses in nm.

To determine the magnetic properties of our films, we utilized broadband ferromagnetic resonance (FMR). The thin film sample was placed face-down on a coplanar

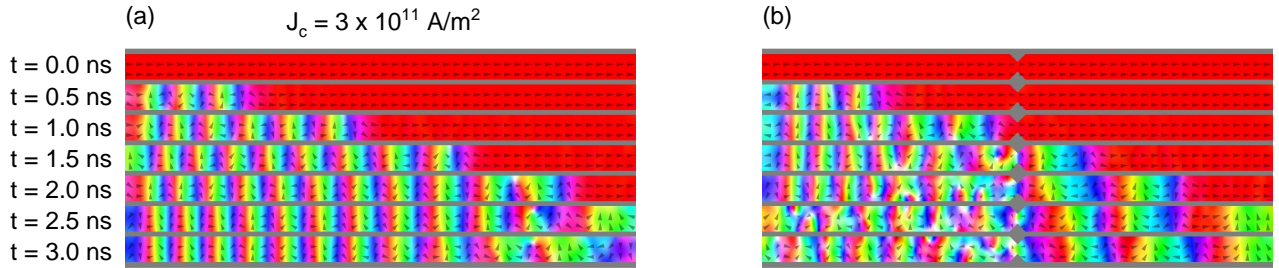


Figure 8. Micromagnetic snapshots of vortex formation in single layer (a) perfect and (b) notched nanostrips

waveguide with a maximum frequency of 36 GHz and magnetized by an external field  $H$  generated by a conventional electromagnet. The FMR spectra was acquired by fixing the microwave frequency and sweeping the magnetic field through the resonance condition. The resulting spectra is then fit with a Lorentzian derivative, from which the resonance field  $H_{res}$  and half-width-at-half-maximum (HWHM) linewidth  $\Delta H$  are determined for each frequency.

The resonance field as a function of microwave frequency is plotted in Fig. 9 and fit using the standard Kittel equation [44]

$$f = \mu_0 \gamma' \sqrt{H_{res}(H_{res} + M_{eff})}, \quad (B1)$$

where  $\gamma' = \gamma/2\pi$  is the reduced gyromagnetic ratio and  $M_{eff}$  is the effective magnetization (here equal to the saturation magnetization  $M_{sat}$ ). From this fit we determine that  $\gamma' \approx 30.5$  GHz/T and  $M_{eff} = 720$  kA/m.

The HWHM linewidth, plotted in Fig. 10, gives insight into the magnetic relaxation of a film. By using the linear equation [45]

$$\Delta H = \Delta H_0 + \frac{\alpha}{\mu_0 \gamma'} f \quad (B2)$$

one can determine the Gilbert damping parameter  $\alpha$  and zero frequency linewidth  $\Delta H_0$ . From the linear fit we deduce  $\alpha = 0.006$  in our 2 nm FeV film.

### Appendix C: Analytical Model Details

The synthetic antiferromagnet (SAF) consists of two identical ferromagnetic nanostrips coupled antiferromagnetically; the nanostrips are labeled by  $i = 1, 2$  and are modeled as quasi-one dimensional spin chains for simplicity. We adopt a coordinate system in which the SAF extends along the  $x$  axis with the strip plane oriented normal to the  $z$  axis. The SAF Hamiltonian can then be written as

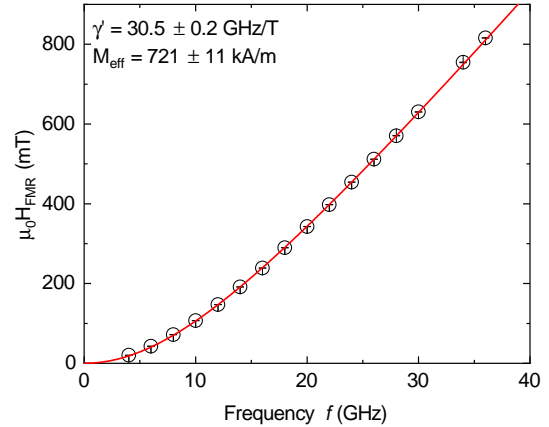


Figure 9. FMR resonance field as a function of microwave frequency. The solid line is a fit according to Eq. B1.

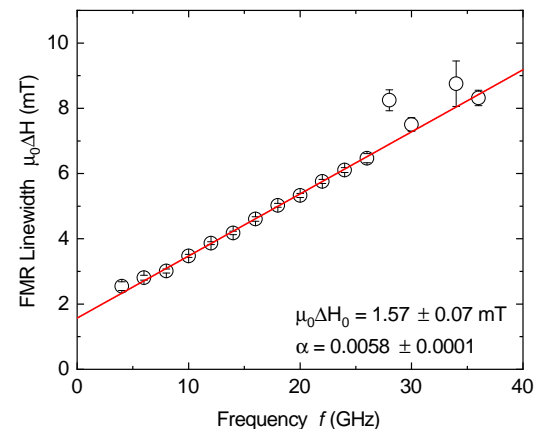


Figure 10. FMR linewidth as a function of microwave frequency. The solid line is a fit according to Eq. B2

$$H_0[\mathbf{n}_i] = \frac{1}{2} \sum_{i=1,2} \int dx [A(\partial_x \mathbf{n}_i(x))^2 + K_{\perp} n_{i,z}^2(x) - K_{\parallel} n_{i,x}^2(x)], \quad (C1)$$

where  $A$  is the exchange stiffness,  $K_{\perp} > 0$  is the easy-plane anisotropy (with the hard axis along the  $z$  axis),  $K_{\parallel} > 0$  is the easy-axis anisotropy along the  $x$  axis, and the unit vector field  $\mathbf{n}_i(x)$  points parallel to the saturated local spin density  $\mathbf{s}_i(x) = s\mathbf{n}_i(x)$ . Finally, we assume the two ferromagnets couple through an isotropic antiferromagnetic exchange interaction described by the Hamiltonian,

$$H_c[\mathbf{n}_i] = \eta \int dx \mathbf{n}_1(x) \cdot \mathbf{n}_2(x). \quad (C2)$$

For low enough excitation energies, DW dynamics in each layer can be described sufficiently in terms of two “soft” variables: the DW position  $X_i(t)$  and the spin canting angle out of the easy ( $xy$ ) plane  $\phi_i(x, t) = \phi_i(t)$ , the latter of which is taken to be uniform along the strip. Focusing exclusively on DWs of the Néel type, an appropriate parametrization for  $\mathbf{n}_i$  in terms of these soft modes is given by [46],

$$\mathbf{n}_i(x, t) = \begin{pmatrix} b_i \tanh\left(\frac{x-X_i(t)}{\lambda}\right) \\ b_i \chi_i \operatorname{sech}\left(\frac{x-X_i(t)}{\lambda}\right) \cos \phi_i(t) \\ \operatorname{sech}\left(\frac{x-X_i(t)}{\lambda}\right) \sin \phi_i(t) \end{pmatrix}, \quad (C3)$$

where  $\lambda = \sqrt{A/K_{\parallel}}$  is the DW width,  $b_i = +1$  ( $b_i = -1$ ) corresponds to tail-to-tail (head-to-head) DW, and  $\chi_i = \pm 1$  is the chirality of the DW. We hereafter fix  $\chi_i = 1$ .

Reduced DW dynamics in terms of the soft variables can be obtained by first inserting Eq. (C3) into the Landau-Lifshitz-Gilbert equation,

$$\dot{\mathbf{n}}_i = \frac{1}{s} \mathbf{n}_i \times \left( -\frac{\delta H}{\delta \mathbf{n}_i} \right) - \alpha \mathbf{n}_i \times \dot{\mathbf{n}}_i, \quad (C4)$$

—  $\alpha$  is the Gilbert parameter — and integrating out the irrelevant fast-oscillating modes by performing a spatial average over Eq. (C4) [47]. The resulting equations are a coupled dynamics for the DWs in the two ferromagnetic nanostrips,

$$\begin{pmatrix} \dot{X}_1 \\ \dot{\phi}_1 \end{pmatrix} = \frac{1}{2(1+\alpha^2)} \begin{pmatrix} \alpha\lambda & -1 \\ 1 & \frac{\alpha}{\lambda} \end{pmatrix} \begin{pmatrix} F_X \\ F_{\phi} \end{pmatrix}, \quad (C5)$$

$$\begin{pmatrix} \dot{X}_2 \\ \dot{\phi}_2 \end{pmatrix} = \frac{1}{2(1+\alpha^2)} \begin{pmatrix} \alpha\lambda & -1 \\ 1 & \frac{\alpha}{\lambda} \end{pmatrix} \begin{pmatrix} -F_X \\ F_{\phi} \end{pmatrix}, \quad (C6)$$

where the force terms read

$$F_X = \frac{2\eta}{s} \left( \frac{\xi}{\sinh^2 \xi} - \coth \xi \right) + \frac{2\eta}{s} \left( \frac{1 - \xi \coth \xi}{\sinh \xi} \right) \cos(\phi_1 + \phi_2), \quad (C7)$$

$$F_{\phi} = -\frac{\lambda K_{\perp}}{s} \sin(2\phi_1) - \frac{2\lambda\eta}{s} \frac{\xi}{\sinh \xi} \sin(\phi_1 + \phi_2), \quad (C8)$$

with  $\xi \equiv (X_1 - X_2)/\lambda$ . For zero interlayer coupling, these equations reduce to the dynamics of two decoupled ferromagnetic DWs, as expected.

Let us now consider the dynamics of a single SAF DW following its injection through the above-described spin-transfer torque mechanism. The injection process may result in differences in the positions and/or canting angles of the two constituent ferromagnetic DWs. Here, we focus on the limit of strong interlayer coupling and strong easy-plane anisotropy such that the injected DW obeys  $X_1 \approx X_2$  and  $\phi_i \ll 1$ .

Upon linearizing Eqs. (C5) and (C6) with respect to  $\xi \ll 1$  and  $\phi_i \ll 1$ , the center-of-mass coordinates  $[\Xi \equiv (X_1 + X_2)/2\lambda$  and  $\Phi \equiv (\phi_1 + \phi_2)/2]$  and the relative coordinates ( $\xi$  and  $\varphi \equiv \phi_1 - \phi_2$ ) decouple, and we arrive at

$$\begin{pmatrix} \dot{\Xi} \\ \dot{\Phi} \end{pmatrix} = \begin{pmatrix} 0 & \gamma_K \\ 0 & -\alpha\gamma_K \end{pmatrix} \begin{pmatrix} \Xi \\ \Phi \end{pmatrix}, \quad (C9)$$

$$\begin{pmatrix} \dot{\xi} \\ \dot{\varphi} \end{pmatrix} = \begin{pmatrix} -\alpha\gamma_{\eta} & \gamma_K \\ -\gamma_{\eta} & -\alpha\gamma_K \end{pmatrix} \begin{pmatrix} \xi \\ \varphi \end{pmatrix}, \quad (C10)$$

where

$$\gamma_{\eta} = \frac{2\eta}{s(1+\alpha^2)}, \quad \gamma_K = \frac{K_{\perp}}{s(1+\alpha^2)}. \quad (C11)$$

Equation (C11) are rates determined by the interlayer exchange and easy-plane anisotropy, respectively.

The dynamics of the relative coordinates (C10) shows that small mismatches in DW positions and canting angles between the top and bottom layers at the time of injection decay on a time scale  $[\alpha(\gamma_{\eta} + \gamma_K)]^{-1}$ . In the limit of very strong interlayer coupling, i.e.,  $\gamma_{\eta} \gg \gamma_K$ , these interlayer mismatches decay on a very short time scale after injection and may effectively be ignored in the DW analysis.

Now focusing on the center-of-mass dynamics (C9), the closed equation for  $\Phi(t)$  may be solved straightforwardly giving

$$\Phi(t) = \Phi_0 e^{-\alpha\gamma_K t}, \quad (C12)$$

<sup>822</sup> Inserting this result into the equation for the DW <sup>825</sup>  
<sup>823</sup> velocity, we find that the velocity decays from its initial <sup>826</sup>  
<sup>824</sup> value over the time scale  $\gamma_K^{-1}$ , i.e.,

$$v(t) \equiv \lambda \dot{\Xi}(t) = \lambda \gamma_K \Phi_0 e^{-\alpha \gamma_K t} . \quad (C13)$$

<sup>827</sup> The rate of DW velocity attenuation is governed by the  
<sup>828</sup> easy-plane anisotropy, i.e.,  $\gamma_K$ . Therefore, in the limit  
<sup>829</sup> of strong interlayer coupling  $\gamma_\eta \gg \gamma_K$ , the velocity  
 decays on a time scale much greater than the time scale  
 governing the decay of the DW's internal mismatch.